CAMBRIDGE
UNIVERSITY PRESS

Article

Xenotime-(Gd), a new Gd-dominant mineral of the xenotime group from the Zimná Voda REE–U–Au quartz vein, Prakovce, Western Carpathians, Slovakia

Martin Ondrejka[1] , Peter Bačík[1,2] , Juraj Majzlan[3] , Pavel Uher[1], Štefan Ferenc[4] , Tomáš Mikuš[5], Martin Števko[2,6] , Mária Čaplovičová[7] , Stanislava Milovská[5] , Alexandra Molnárová[2], Christiane Rößler[8] and Christian Matthes[8]

[1]Department of Mineralogy, Petrology and Economic Geology, Faculty of Natural Sciences, Comenius University, Ilkovičova 6, Mlynská dolina, 842 15, Bratislava, Slovakia; [2]Earth Science Institute, Slovak Academy of Sciences, Dúbravská cesta 9, 840 05, Bratislava, Slovakia; [3]Institute of Geosciences, Friedrich Schiller University, Burgweg 11, 07749 Jena, Germany; [4]Department of Geography and Geology, Faculty of Natural Sciences, Matej Bel University, Tajovského 40, 974 01 Banská Bystrica, Slovakia; [5]Earth Science Institute, Slovak Academy of Sciences, Ďumbierska 1, 974 01, Banská Bystrica, Slovakia; [6]Department of Mineralogy and Petrology, National Museum, Cirkusová 1740, 193 00 Praha-Horní Počernice, Czech Republic; [7]Centre for Nanodiagnostics of Materials, Faculty of Materials Science and Technology, Slovak University of Technology, Vazovova 5, 812 43 Bratislava, Slovakia; and [8]Bauhaus University, Coudraystrasse 11, 99423 Weimar, Germany

Abstract

Xenotime-(Gd), ideally $GdPO_4$, is a new mineral of the xenotime group. It was discovered at the Zimná Voda REE–U–Au occurrence near Prakovce, Western Carpathians, Slovakia. It forms rare crystal domains (≤ 20 μm, usually ≤ 10 μm in size) in Gd-rich xenotime-(Y) crystals (≤ 100 μm in size), in association with monazite-group minerals, uraninite, fluorapatite and uranyl arsenates–phosphates. The hydrothermal REE–U–Au mineralisation occurs in a quartz–muscovite vein, hosted in Palaeozoic phyllites near exocontact with Permian granites. The density is 5.26 g/cm^3, based on calculated average empirical formula and unit-cell parameters. The average chemical composition ($n = 6$) measured by electron microprobe is as follows (wt.%): P_2O_5 30.1, As_2O_5 0.5, SiO_2 0.2, UO_2 0.3, Y_2O_3 15.7, (La, Ce, Pr, Nd)$_2O_3$ 0.5, Sm_2O_3 5.7, Eu_2O_3 1.4, Gd_2O_3 29.2, Tb_2O_3 3.9, Dy_2O_3 10.4, Ho_2O_3 0.4, (Er, Tm, Yb, Lu)$_2O_3$ 2.1, (Ca, Fe, Pb, Mn, Ba)O 0.1, total 100.5. The corresponding empirical formula calculated on the basis of 4 oxygen atoms is: $(Gd_{0.37}Y_{0.32}Dy_{0.13}Sm_{0.08}Tb_{0.05}Eu_{0.02}Er_{0.01}Tm_{0.01}Nd_{0.01}...)_{\Sigma1.01}(P_{0.98}As_{0.01}Si_{0.01})O_4$. The empirical formula of the Gd-richest composition is: $(Gd_{0.38}Y_{0.31}Dy_{0.13}Sm_{0.08}Tb_{0.05}Eu_{0.02}Er_{0.01}Nd_{0.01}Ho_{0.01}...)_{\Sigma1.01}(P_{0.98}As_{0.01}Si_{0.01})O_4$. The ideal formula is $GdPO_4$. The xenotime-type structure has been confirmed by micro-Raman spectroscopy and a Fast Fourier-Transform pattern using HRTEM. Xenotime-(Gd) is tetragonal, space group $I4_1/amd$, $a = 6.9589(5)$ Å, $c = 6.0518(6)$ Å, $V = 293.07(3)$ Å^3 and $Z = 4$. The new mineral is named as an analogue of xenotime-(Y) and xenotime-(Yb) with Gd dominant among the REE. The middle REE enrichment of xenotime-(Gd) is shared with the associated monazite-(Gd) and Gd-rich hingganite-(Y). This exotic REE signature and precipitation of Gd-bearing minerals is a product of selective complexing and enrichment in MREE in low-temperature hydrothermal fluids by alteration of uraninite, brannerite and fluorapatite on a micro-scale. The existence of xenotime-(Gd) and monazite-(Gd) is the first naturally documented dimorphism among REE phosphates. In addition, xenotime-(Gd) is only the third approved Gd-dominant mineral, after lepersonnite-(Gd) and monazite-(Gd).

Keywords: xenotime-(Gd); new mineral; xenotime group; gadolinium; rare earth elements; Prakovce-Zimná Voda; Western Carpathians; Slovakia

(Received 4 March 2024; accepted 18 August 2024)

Introduction

Rare earth elements (REE) represent a unique set of elements having coherent behaviour and very similar properties which are responsible for their similar geochemistry. The International

Union of Pure and Applied Chemistry (IUPAC) definition of the REE group includes lanthanides (Ln), yttrium (Y) and scandium (Sc). However, due to the substantially smaller ionic radius of Sc^{3+} with respect to the rest of the group, Sc frequently enters different structural sites, and therefore Sc is commonly not included into the REE in natural geological environments. Due to the lanthanide contraction phenomenon, the REE are further divided into larger LREE (light Ln, La–Sm), medium MREE (Sm–Dy) and smaller HREE (heavy Ln, Tb–Lu and Y).

Minerals belonging to the xenotime group are anhydrous orthophosphates, orthoarsenates and orthovanadates with tetragonal symmetry and space group $I4_1/amd$ (#141). Among

phosphates, xenotime-(Y) is the most common species and contains predominantly Y^{3+} and usually low contents of other HREE as well as negligible amounts of LREE based on their preference of the xenotime-type crystal structure (cf. Ni *et al.*, 1995). On the other hand, xenotime-(Yb) and Yb-, Dy- and Gd-rich xenotime-(Y) are rare minerals occurring in some granitic pegmatites and metamorphic-hydrothermal lithologies (Demartin *et al.*, 1991; Förster and Rhede, 1995; Franz *et al.*, 1996; Förster, 1998; Buck *et al.*, 1999; Masau *et al.*, 2000; Repina, 2011; Repina *et al.*, 2014; Franz *et al.*, 2015; Ondrejka *et al.*, 2023b, 2023c).

In contrast to numerous minerals with REE as their essential constituents (particularly Ce and Y, more rarely La, Nd, Sm and Yb), there are currently only two Gd-dominant minerals approved by the International Mineralogical Association, Commission on New Minerals, Nomenclature and Classification (IMA-CNMNC, Pasero, 2024): lepersonnite-(Gd) $CaGd_2(UO_2)_{24}(SiO_4)_4(CO_3)_8(OH)_{24}\cdot48H_2O$, a rare REE-uranyl carbonate from the Shinkolobwe U deposit in the DR Congo (Deliens and Piret, 1982) and monazite-(Gd) (Ondrejka *et al.*, 2023b) which is cogenetic with the xenotime-(Gd) described here.

In this work, we describe a new Gd-dominant mineral xenotime-(Gd), discovered in a hydrothermal quartz vein with REE−U−Au mineralisation at the Zimná Voda occurrence near Prakovce, Slovakia. Xenotime-(Gd) is a new Gd-dominant member of the xenotime group and it is related to xenotime-(Y) and xenotime-(Yb) by substitution of Gd for other REEs, having the REE composition distinctly shifted towards the MREE enrichment. The new mineral and its name have been approved by the IMA-CNMNC (IMA 2023-091; Ondrejka *et al.*, 2024) and the Levinson modifier for rare earth minerals (Levinson, 1966; Bayliss and Levinson, 1988). The symbol Xtm-Gd was given to the new mineral. The holotype specimen of xenotime-(Gd) (FIB lamella of the thin section ZV-2A4) is deposited in the collection of the Slovak National Museum, Natural History Museum, Vajanského nábrežie 2, P.O. BOX 13, 810 06 Bratislava, Slovak Republic under the catalogue number M-20412. The crystallographic information file (cif) is deposited in American Mineralogist Crystal Structure Database (AMCSD; Downs and Hall-Wallace, 2003) under the code 0021444 and is also available as Supplementary material (see below).

Occurrence

The Zimná Voda REE−U−Au occurrence was discovered in 1975, during exploration for uranium ores (Novotný and Čížek, 1979). The sample containing xenotime-(Gd) was collected by the authors in September 2017 during reconnaissance of the Zimná Voda REE−U−Au quartz vein, Prakovce, Gelnica Co., eastern Slovakia. The site is located near the main ridge of the Slovenské Rudohorie Mts., ∼5.6 km to the S of the Prakovce village, 600 m to the NW of the Tri Studne elevation point (969 m a.s.l.) and 400 m NW of Trohánka bivouac shelter, at an altitude of ∼950 m a.s.l., ca. 23 km WNW of Košice town at 48.7666°N, 20.9137°E.

The hydrothermal REE−U−Au vein mineralisation at the Zimná Voda occurrence is hosted in the Lower Palaeozoic metamorphic rocks of the Bystrý Potok Formation, a part of the Gelnica Group in the Gemeric tectonic unit of the Western Carpathians, which is part of the Alpine-Carpathian Mountain belt (Bajaník *et al.*, 1983; Ivanička *et al.*, 1989). Two quartz veins (Western and Eastern) containing REE, U and Au mineralisation were found in the area. Xenotime-(Gd) was found in the

Western vein. The vein is hosted in fine-grained micaceous phyllites interbedded with fine-grained quartzites. It has an E−W strike, total length of ∼90 m with an average dip of 65° to the S, and conforms to the schistosity of the host rocks. The thickness of the vein ranges from 3 to 30 cm. Along the contact, the rocks are intensively argillitised, and locally silicified, and impregnated by pyrite. Supergene alteration of pyritised rocks caused their limonitisation.

The metamorphic rocks were intruded by Hummel granites which outcrop 600 m to the SW of the investigated occurrence. These igneous rocks are leucocratic peraluminous rare-metal granites with S-type affinity and relatively high degree of magmatic fractionation, evidenced by higher P concentrations in K-feldspar and elevated contents of rare lithophile elements (Li, Rb, Cs, B, Sn, W, Nb and Ta) and F. They originated and were emplaced during the post-Variscan, Permian (260−270 Ma) extension stage (e.g. Villaseñor *et al.*, 2021, and references therein).

In addition to xenotime-(Gd), the following minerals were identified in the Western vein: arsenopyrite, native bismuth, bismuthinite, brannerite, chlorite, cobaltite, fluorapatite, galena, gersdorffite, glaucodot, native gold, hingganite-(Y), kobellite, pyrite, quartz, molybdenite, monazite-(Ce), monazite-(Gd), monazite-(Nd), monazite-(Sm), muscovite, rutile, stibnite, tetrahedrite-(Fe), tintinaite, tourmaline-group minerals, uraninite and xenotime-(Y); supergene minerals are represented by arseniosiderite, goethite and other undifferentiated iron oxyhydroxides, pharmacosiderite–bariopharmacosiderite, philipsbornite–segnitite, scorodite, zeunerite, other uranyl arsenates–phosphates (most abundant are kahlerite, nováčekite, threadgoldite, rarely arsenuranospathite, autunite, chistyakovaite related mineral phases and phosphuranylite); Ondrejka *et al.* (2023a, 2023b, 2023c). The mineralisation probably originated by fluid-driven hydrothermal mobilization of REE, U and Au from the surrounding metamorphic rocks induced by the intrusion of the granitic rocks (Rojkovič *et al.*, 1997; 1999). The perigranitic origin is supported by the age correlation of uraninite (246–265 Ma), the geochemical signatures and the spatial proximity of the mineralised veins with Permian rare-metal granites of the Gemeric Unit (cf. Kohút and Stein, 2005; Ferenc *et al.*, 2021; Ondrejka *et al.*, 2023c). Further details and regional geology can be found in Ondrejka *et al.* (2023c).

Experimental methods

The chemical composition of xenotime-(Gd) was studied by a JEOL JXA-8530F electron probe microanalyser (EPMA) in the wavelength-dispersive spectrometry (WDS) mode at the Earth Science Institute, Slovak Academy of Sciences in Banská Bystrica, Slovakia. An accelerating voltage of 15 kV and a probe current of 20 nA were used. The typical spot beam diameter varied from 2 to 6 μm; a more focused ≤1−3 μm beam was used only occasionally to avoid any intermediate composition in strongly heterogeneous micro-scale areas. The determination was calibrated using natural and synthetic calibrants (Table 1), and raw counts were converted to wt.% of oxides using the ZAF matrix correction. Corrections of line interferences were provided using the method by Åmli and Griffin (1975). The detection limit for all elements is typically between 0.01 and 0.15 wt.%. Element contents in the mineral formula are expressed in atoms per formula unit (apfu). The xenotime-(Gd) formula was normalised to 4 oxygen atoms.

Table 1. Conditions used for the electron microprobe analyses.

Element	Line	Crystal	Standard	Detect. limit (3σ) in ppm Xtm-Gd
S	$K\alpha$	PETL	baryte	100–110
P	$K\alpha$	PETL	apatite	205–215
As	$L\alpha$	TAP	GaAs	1190–1205
Si	$K\alpha$	TAP	albite	205–215
Th	$M\alpha$	PETL	thorianite	290–300
U	$M\beta$	PETL	UO_2	400–415
Al	$K\alpha$	TAP	albite	165–175
Y	$L\alpha$	PETL	YPO_4	300–315
La	$L\alpha$	LIFH	$LaPO_4$	390–400
Ce	$L\alpha$	LIFH	$CePO_4$	360–370
Pr	$L\beta$	LIFH	$PrPO_4$	680–690
Nd	$L\alpha$	LIFH	$NdPO_4$	350–360
Sm	$L\beta$	LIFH	$SmPO_4$	735–745
Eu	$L\alpha$	LIFH	$EuPO_4$	370–380
Gd	$L\beta$	LIFH	$GdPO_4$	400–410
Tb	$L\alpha$	LIFH	$TbPO_4$	425–435
Dy	$L\alpha$	LIFH	$DyPO_4$	445–455
Ho	$L\beta$	LIFH	$HoPO_4$	985–1000
Er	$L\alpha$	LIFH	$ErPO_4$	480–490
Tm	$L\alpha$	LIFH	$TmPO_4$	515–525
Yb	$L\alpha$	LIFH	$YbPO_4$	540–550
Lu	$L\alpha$	LIFH	$LuPO_4$	565–580
Ca	$K\alpha$	PETL	diopside	95–110
Fe	$K\alpha$	LIF	hematite	630–640
Mn	$K\alpha$	LIF	rhodonite	495–505
Pb	$M\alpha$	PETL	crocoite	410–420
Ba	$L\alpha$	LIF	baryte	1385–1410
Na	$K\alpha$	TAP	albite	300–310

Depolarised Raman measurements were conducted on an unoriented section of xenotime-(Gd) using a Labram HR800 spectrometer (Horiba Jobin-Yvon), which was linked to an Olympus-BX41 optical microscope (Earth Science Institute, Slovak Academy of Sciences in Banská Bystrica, Slovakia). The samples were exposed to 532 nm frequency-doubled Nd-YAG and 633 nm He–Ne lasers. The system resolution was ~2 cm^{-1}.

Slicing and polishing of a lamella for electron diffraction analysis were carried out using a scanning electron microscope (SEM) coupled with a gallium-focused ion beam (FIB) source (Bauhaus University Weimar, Germany). The SEM-FIB (Helios G4 UX, ThermoFisherScientific) is equipped with a high-performance FIB source (Phoenix) that allows the polishing of TEM lamella at very low acceleration voltage or beam current. This feature is essential for obtaining undisturbed thin lamella suitable for high-resolution TEM imaging. Thin sections of samples, as used for optical light microscopic investigation and other analyses, were sputtered with an ≈ 8 nm gold layer to ensure the electric conductivity of the full sample and to reduce sample abrasion during ion beam imaging. Sites for extraction of the lamellae were selected according to previous microscopic and spectroscopic characterisation of the samples. Areas of interest were covered with an approximately 15×3×3 µm layer of platinum to further protect the sample surface against ion beam damage.

Transmission electron microscopy (TEM), high-resolution TEM (HRTEM), and scanning transmission electron microscopy (STEM) characterisations were performed using double corrected TEM/STEM JEOL JEM-ARM200CF (JEOL Ltd., Tokyo, Japan) with cold-FEG cathode operated at 200 kV located in the Centre for Nanodiagnostics of Materials, Faculty of Materials Science and Technology, Slovak University of Technology in Bratislava, Slovakia.

Images from HRTEM were recorded using a Gatan Orius SC1000 CCD Camera (Gatan Inc., Pleasanton, CA, USA) with a resolution of 2048 × 2048 pixels using the *DigitalMicrograph* software package (version 3.60.4435.0, Gatan Inc., Pleasanton, CA, USA). The measurement of the reflection positions and angles in Fast Fourier Transform (FFT) patterns acquired from relevant HRTEM images was done using the DIFPACK module incorporated in *DigitalMicrograph* software. By clicking on the spots on the FFT pattern DIFPACK locates the spots at the brightest pixel value precisely.

A high-angle annular dark field (HAADF) STEM detector with inner-collection semi-angle of 90 mrad, and a probe convergence semi-angle of 22 mrad were utilised to obtain atomic resolution HAADF STEM images. Crystal structure simulations were carried out using *CrystalMaker*® for Windows version 2.3.0 (Begbroke, UK).

Appearance and physical properties

Xenotime-(Gd) forms rare crystal domains or zones (≤20 µm in size, usually ≤10 µm), in Gd-rich xenotime-(Y) crystals (≤100 µm in size, xenotime II, Ondrejka *et al.*, 2023c) in close association with Gd-poor xenotime-(Y) (xenotime I, ibidem), monazite-group minerals, particularly monazite-(Gd) and monazite-(Sm), uraninite, supergene uranyl arsenates and phosphates, dispersed in quartz–muscovite gangue (Fig. 1a). The holotype specimen (FIB lamella) is positioned in the Gd-richest domain of the xenotime crystal (Fig. 1b–d). Among two xenotime-group species recognised in the Western vein at Zimná Voda occurrence, xenotime-(Y) is the most common and occurs in all of 6 samples studied (ZV-1 to ZV-6). Xenotime-(Gd) was found only in the ZV-2 sample and unlike monazite-(Gd) with occurrence in multiple thin sections, xenotime-(Gd) was found only in the thin section ZV-2A4. The lustre, hardness, cleavage and parting of xenotime-(Gd) could not be determined, nor could density be measured due to an insufficient quantity of mineral for physical measurement. We assume, however, that these properties are similar to those observed in other xenotime-group minerals. The density of 5.26 g/cm^3 was calculated on the basis of the average empirical formula and calculated unit-cell volume (see below). The density of the ideal xenotime-structured formula $GdPO_4$ is 5.66 g cm^{-3} (Rodriguez-Liviano *et al.*, 2013) to 5.77 g cm^{-3} (Ni *et al.*, 1995) calculated from the unit-cell volume of synthetic $GdPO_4$ due to the significant presence of lighter elements, mostly Y. In comparison, the density of natural xenotime-(Y) varies between 4.4 and 5.1 g cm^{-3} (Anthony *et al.*, 2024). Optical properties could not be determined because of the small sample size, but they are probably similar to other xenotime-group minerals. The value of $n = 1.87$ calculated from the Gladstone-Dale relationship (Mandarino, 1979, 1981) using an empirical formula and calculated density of the holotype specimen is slightly higher than the refractive index of natural xenotime-(Y), which is up to 1.83 (Anthony *et al.*, 2024) due to enrichment in heavier REE.

Chemical composition

Chemical analyses were carried-out on crystals in the ZV-2A4 thin section and are positioned within and in close vicinity of the FIB lamella holotype specimen (Fig. 1b). The representative chemical composition is shown in Table 2. The xenotime-(Gd) µm-scale domains are chemically relatively homogeneous, with no distinct variations in the Y/Gd mass ratio (0.47–0.50).
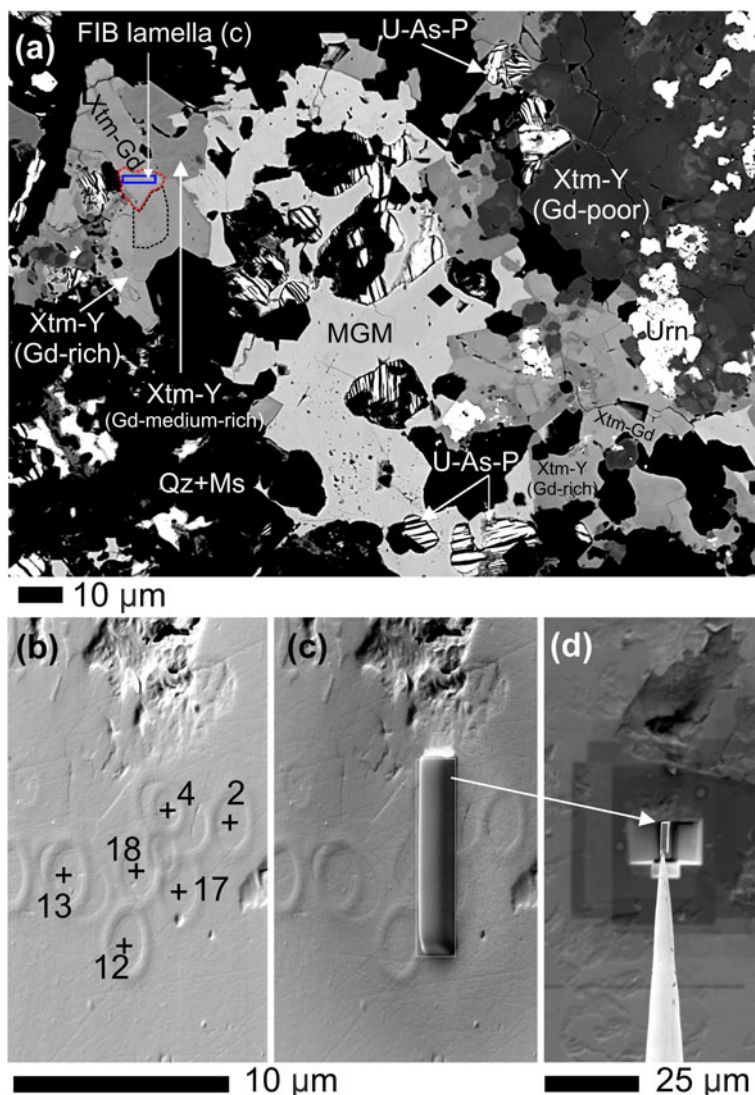
Figure 1. Back-scattered electron images (BSEI) of (a) a large aggregate of monazite-group minerals (MGM) with xenotime-(Gd) (Xtm-Gd), xenotime-(Y) (Xtm-Y), uraninite (Urn) and uranyl arsenates-phosphates (U-As-P) in quartz-muscovite gangue (Qz + Ms). The red dashed area indicates the Gd-richest (Gd-apfu-dominant) composition Gd_2O_3>29 wt.%; Y_2O_3<16 wt.%; black dashed area indicates Gd-rich (Gd-apfu-dominant) Gd_2O_3=28–29 wt.%. The position of the holotype FIB lamella (#M-20412) is documented herein. (b) The spot positions of electron microprobe analyses in Table 2. (c) The FIB lamella (holotype specimen) positioned in the Gd-richest domain of the xenotime crystal. (d) The extraction of the FIB lamella from the sample. Mineral symbols from Warr (2021). Note: Images (b), (c) and (d) are rotated 90 degrees to the view in (a).

However, those Gd-dominant domains are always a part of a larger and heterogeneous Gd-rich to Gd-medium-rich xenotime-(Y) with Y/Gd = 0.56–2.57. The analysed domains have a composition with Gd>Y>Dy > Sm > Tb (28.5–29.3 wt.% Gd_2O_3, 0.36–0.38 apfu Gd; 15.2–16.1 wt.% Y_2O_3, 0.31–0.33 apfu Y; 10.1–10.8 wt.% Dy_2O_3, 0.13 apfu Dy; 5.3–6.2 wt.% Sm_2O_3, 0.07–0.08 apfu Sm; 3.7–4.0 wt.% Tb_2O_3, 0.05 apfu Tb). The average chemical composition of xenotime-(Gd) calculated from six point electron-microprobe analyses is as follows (wt.%): %): P_2O_5 30.1, As_2O_5 0.5, SiO_2 0.2, UO_2 0.3, Y_2O_3 15.7, $(La, Ce, Pr, Nd)_2O_3$ 0.5, Sm_2O_3 5.7, Eu_2O_3 1.4, Gd_2O_3 29.2, Tb_2O_3 3.9, Dy_2O_3 10.4, Ho_2O_3 0.4, $(Er, Tm, Yb, Lu)_2O_3$ 2.1, $(Ca, Fe, Pb, Mn, Ba)O$ 0.1, total 100.5. The corresponding empirical formula calculated on the basis of 4 oxygen atoms is: $(Gd_{0.37}Y_{0.32}Dy_{0.13}Sm_{0.08}Tb_{0.05}Eu_{0.02}Er_{0.01}Tm_{0.01}Nd_{0.01}...)_{\Sigma1.01}(P_{0.98}As_{0.01}Si_{0.01})O_4$. The empirical formula of xenotime-(Gd) in its Gd-richest spot is: $(Gd_{0.38}Y_{0.31}Dy_{0.13}Sm_{0.08}Tb_{0.05}Eu_{0.02}Er_{0.01}Nd_{0.01}Ho_{0.01}...)_{\Sigma1.01}(P_{0.98}As_{0.01}Si_{0.01})O_4$ which leads to the end-member formula $GdPO_4$ requiring (in wt.%): Gd 62.35, P 12.28, and O 25.37, or Gd_2O_3 71.86, P_2O_5 28.14, total 100.00 wt.%.

In general, the element distribution shows enrichment towards the MREE, depletion of HREE+Y and negligible LREE abundances. The chondrite-normalised patterns exhibit conspicuous maxima at Gd and Tb (MREE hump; for further details, see Ondrejka *et al.*, 2023c). The concentration of Th was usually below the detection limit of the EPMA; U attains only 0.4 wt.% UO_2 (0.004 apfu U). Arsenic is always present (≤0.7 wt.% As_2O_5, 0.014 apfu As) and attests to limited PAs_{-1} (chernovite) substitution. Satisfactory analytical totals $(99 − 101$ wt.%), excellent stoichiometry calculated on an anhydrous basis and Raman spectra (see below) indicate that a potential role of a tetrahedral array of $(OH)^-$ groups is negligible, if any. Other trace elements (Ca, Sr, Fe, Pb, Si, F and S) have negligible concentrations or are below detection limits (Table 2).

Crystallography

Xenotime-(Gd) is isostructural with other xenotime-group minerals; its tetragonal (space group $I4_1/amd$) structure consists of isolated PO_4 tetrahedra separated by intervening $(REE)O_8$ polyhedra. A smaller REE-containing polyhedron in the xenotime structure with the 8-fold coordination compared to a monoclinic monazite structure with the 9-fold coordination accommodates the smaller cations; therefore, the xenotime structure prefers HREE over

Table 2. Representative and average EPMA data and mineral formula of xenotime-(Gd). Spot numbers correspond to positions on Fig. 1.

Wt.%	2	4	12	13	17	18	Mean (*n* = 6)	apfu	2	4	12	13	17	18	Mean (*n* = 6)
SO_3	0.00	0.00	0.02	0.02	0.00	0.00	0.01	S^{6+}	0.000	0.000	0.001	0.001	0.000	0.000	0.000
P_2O_5	29.90	30.60	29.77	29.95	30.02	30.45	30.11	P^{5+}	0.981	0.987	0.970	0.974	0.977	0.988	0.980
As_2O_5	0.40	0.48	0.71	0.71	0.69	0.26	0.54	As^{5+}	0.008	0.010	0.014	0.014	0.014	0.005	0.011
SiO_2	0.19	0.05	0.26	0.19	0.22	0.26	0.19	Si^{4+}	0.007	0.002	0.010	0.007	0.009	0.010	0.007
ThO_2	0.00	0.00	0.00	0.04	0.00	0.00	0.01	Th^{4+}	0.000	0.000	0.000	0.000	0.000	0.000	0.000
UO_2	0.28	0.23	0.37	0.31	0.24	0.42	0.31	U^{4+}	0.002	0.002	0.003	0.003	0.002	0.004	0.003
Al_2O_3	0.00	0.00	0.00	0.00	0.00	0.00	0.00	Al^{3+}	0.000	0.000	0.000	0.000	0.000	0.000	0.000
Y_2O_3	15.24	15.72	15.82	16.11	15.59	15.92	15.73	Y^{3+}	0.314	0.319	0.324	0.329	0.319	0.325	0.322
La_2O_3	0.05	0.06	0.07	0.10	0.08	0.04	0.06	La^{3+}	0.001	0.001	0.001	0.001	0.001	0.000	0.001
Ce_2O_3	0.02	0.04	0.00	0.00	0.01	0.00	0.01	Ce^{3+}	0.000	0.001	0.000	0.000	0.000	0.000	0.000
Pr_2O_3	0.09	0.00	0.00	0.00	0.00	0.00	0.01	Pr^{3+}	0.001	0.000	0.000	0.000	0.000	0.000	0.000
Nd_2O_3	0.47	0.41	0.40	0.54	0.49	0.35	0.44	Nd^{3+}	0.007	0.006	0.006	0.007	0.007	0.005	0.006
Sm_2O_3	6.05	6.15	5.26	5.34	5.77	5.44	5.67	Sm^{3+}	0.081	0.081	0.070	0.071	0.076	0.072	0.075
Eu_2O_3	1.39	1.46	1.45	1.36	1.40	1.49	1.43	Eu^{3+}	0.018	0.019	0.019	0.018	0.018	0.020	0.019
Gd_2O_3	29.22	29.30	29.16	29.24	29.22	28.82	29.16	Gd^{3+}	0.376	0.370	0.372	0.372	0.372	0.366	0.371
Tb_2O_3	3.74	3.85	3.99	3.87	3.84	3.86	3.86	Tb^{3+}	0.048	0.048	0.050	0.049	0.048	0.049	0.049
Dy_2O_3	10.13	10.39	10.53	10.41	10.25	10.50	10.37	Dy^{3+}	0.126	0.128	0.131	0.129	0.127	0.130	0.128
Ho_2O_3	0.48	0.46	0.55	0.05	0.15	0.45	0.36	Ho^{3+}	0.006	0.006	0.007	0.001	0.002	0.006	0.004
Er_2O_3	0.92	0.62	1.06	1.03	1.02	0.48	0.86	Er^{3+}	0.011	0.007	0.013	0.012	0.012	0.006	0.010
Tm_2O_3	0.87	0.94	0.87	0.87	0.92	0.85	0.89	Tm^{3+}	0.010	0.011	0.010	0.010	0.011	0.010	0.011
Yb_2O_3	0.29	0.37	0.06	0.26	0.28	0.27	0.25	Yb^{3+}	0.003	0.004	0.001	0.003	0.003	0.003	0.003
Lu_2O_3	0.08	0.09	0.08	0.08	0.08	0.07	0.08	Lu^{3+}	0.001	0.001	0.001	0.001	0.001	0.001	0.001
FeO_t	0.00	0.00	0.00	0.00	0.00	0.00	0.00	Fe^{2+}	0.000	0.000	0.000	0.000	0.000	0.000	0.000
PbO	0.08	0.00	0.00	0.00	0.00	0.03	0.02	Pb^{2+}	0.001	0.000	0.000	0.000	0.000	0.000	0.000
MnO	0.02	0.00	0.11	0.00	0.00	0.06	0.03	Mn^{2+}	0.001	0.000	0.004	0.000	0.000	0.002	0.001
CaO	0.01	0.00	0.00	0.01	0.00	0.00	0.00	Ca^{2+}	0.001	0.000	0.000	0.000	0.000	0.000	0.000
BaO	0.00	0.00	0.20	0.00	0.19	0.00	0.07	Ba^{2+}	0.000	0.000	0.003	0.000	0.003	0.000	0.001
Na_2O	0.00	0.00	0.00	0.00	0.00	0.00	0.00	Na^+	0.000	0.000	0.000	0.000	0.000	0.000	0.000
Total	99.92	101.22	100.76	100.47	100.48	100.02	100.47	Σ*A**	1.008	1.003	1.014	1.008	1.004	0.997	1.006
Y/Gd (mass)	0.47	0.49	0.49	0.50	0.48	0.50	0.49	Σ*B**	0.996	0.999	0.994	0.996	0.999	1.003	0.998
								Σ*AB*	2.005	2.001	2.008	2.004	2.004	2.001	2.004

*Note: Σ*A* = sum of cations at the *A* site (Th+U+Al+REE+Fe+Pb+Mn+Ca+Ba+Na); Σ*B* = sum of cations at the *B* site (S+P+As+Si).

MREE and LREE (e.g. Miyawaki and Nakai, 1993; Ni *et al.*, 1995). Consequently, xenotime crystals with MREE enrichment are rare.

To determine the crystal structure of the mineral, HRTEM and STEM characterisation on focused ion beam (FIB) lamella was used. This procedure enables measurement of the same phases that were previously analysed by EPMA. A single-crystal X-ray diffraction study of xenotime-(Gd) was not carried out due to the small size of the crystals. Powder X-ray diffraction data could also not be obtained, but because the xenotime structure of synthetic $GdPO_4$ is known (tetragonal, space group $I4_1/amd$, $a = 6.9648(4)$ Å and $c = 6.1050(5)$ Å; Rodriguez-Liviano *et al.*, 2013; $a = 6.9612(7)$ Å and $c = 6.1026(10)$ Å (Clavier *et al.*, 2018), a pattern was calculated using the cif (Table 3). The xenotime structure can be described as [001]-oriented chains formed of alternating phosphate tetrahedra and REE polyhedra (Vegard, 1927). Each PO_4 tetrahedron is isolated from other PO_4 tetrahedra and shares two of its edges with the $REEO_8$ polyhedra. In synthetic $GdPO_4$, the smaller P^{5+} cations are tetrahedrally coordinated with a P–O bond length of 1.554(4) Å and two different OPO angles [101.6(3)° and 113.6(2)°]. The PO_4 tetrahedra are connected to Gd^{3+} cations with coordination number 8 and two unique Gd–O bond lengths [2.343(4) and 2.397(4) Å] (Rodriguez-Liviano *et al.*, 2013). Therefore, a HRTEM with FFT techniques was used to determine the unit-cell parameters of the crystal examined.

A thin lamella of a xenotime-(Gd) single crystal was tilted in the electron microscope to obtain a low-index zone axis parallel to the primary electron beam. At this setting, HRTEM resulted in the recording of a defect-free single crystalline structure (Fig. 2a). The corresponding FFT pattern was acquired from the

entire recorded area and the interplanar distances obtained by measuring the reflection positions and the angles between individual reflections were determined (Fig. 2b). Using this method, a set of 25 reflections were measured using FFT and with refinement gave the following unit-cell parameters: $a = 6.9589(5)$ Å, $c = 6.0518(6)$ Å, $V = 293.07(3)$ Å^3 and $Z = 4$.

The measured angles and interplanar distances were compared with relevant data obtained using a standard stereographic

Table 3. Calculated powder X-ray diffraction pattern (λ = 1.5406 Å) for xenotime-(Gd) compared to synthetic xenotime-(Gd) (Rodriguez-Liviano *et al.*, 2013).*

	Xenotime-(Gd) - holotype			Synthetic xenotime-(Gd)		
hkl	2θ	*d* (Å)	100·*I*/*I*$_{max}$	2θ	*d* (Å)	100·*I*/*I*$_{max}$
011	19.423	4.5665	43	19.304	4.5942	100
020	25.581	3.4794	100	25.551	3.4835	2
121	32.321	2.7676	18	32.223	2.7758	20
112	34.777	2.5776	63	34.513	2.5967	2
220	36.491	2.4603	19	36.447	2.4632	38
022	39.433	2.2833	4	39.186	2.2971	15
031	41.665	2.1660	20	41.567	2.1709	12
013	46.853	1.9375	13	46.404	1.9552	4
231	49.532	1.8388	19	49.429	1.8424	8
132	51.293	1.7797	53	51.067	1.7871	0
040	52.562	1.7397	14	52.496	1.7418	17
123	54.137	1.6928	8	53.717	1.7050	11
141	56.564	1.6257	5	56.455	1.6286	7
240	59.344	1.5561	11	59.268	1.5579	0

*The data were calculated with the program *Diamond*, v 4.0, for the composition and unit-cell parameters of the natural sample investigated in this work.
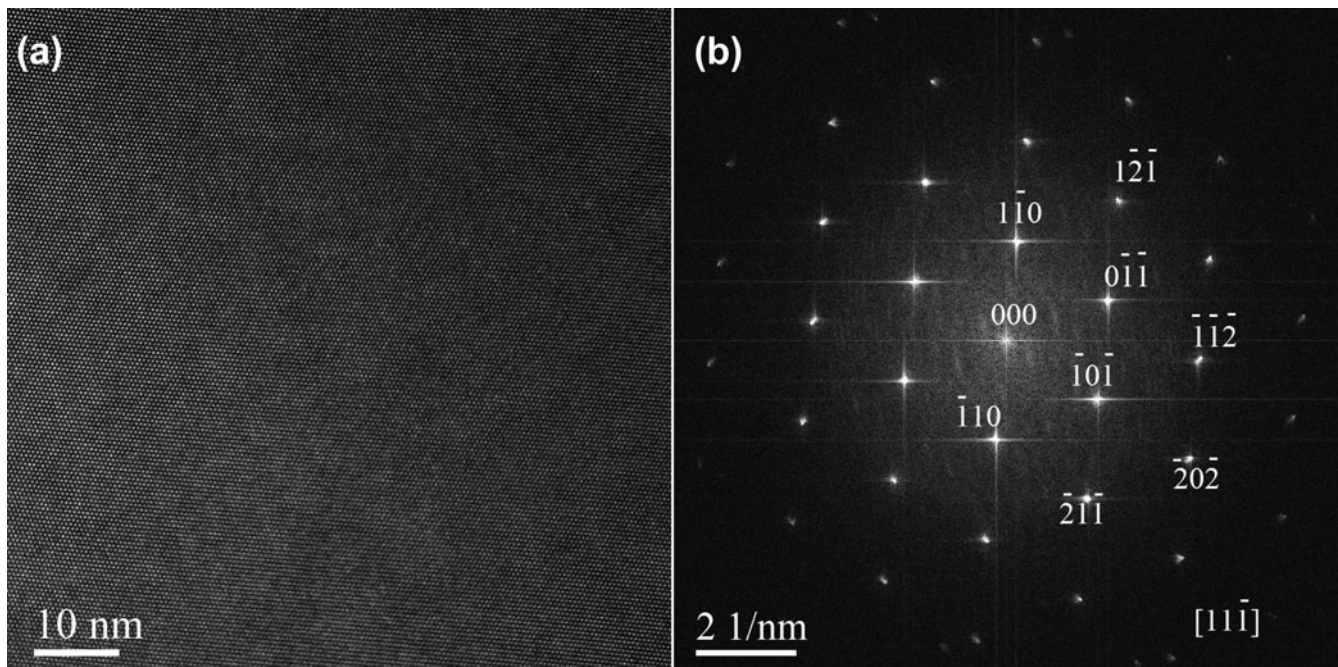
Figure 2. (a) High-resolution TEM image of the crystal lattice viewed along the [11$\bar{1}$] direction. (b) Relevant FFT pattern showing the [11$\bar{1}$] zone axis.

projection of the tetragonal crystal of xenotime-(Gd) (Rodriguez-Liviano et al., 2013). Based on this, and also using the rules for indexing point electron diffractions, Miller indices were assigned to all reflections in the FFT pattern (Fig. 2b).

The experimentally obtained d-spacings of 0.5001 nm and 0.457 nm are in good agreement with that of 0.49015 nm and 0.45664 nm, respectively, reported for interplanar distances of ($\bar{1}$10) and ($\bar{1}$0$\bar{1}$) planes of tetragonal xenotime-(Gd) (Rodriguez-Liviano et al., 2013). Moreover, the measured angle of 62.90° between these reflections corresponds well with the 62.23° valid

for the angle between ($\bar{1}$10) and ($\bar{1}$0$\bar{1}$) planes according to standard stereographic projection of xenotime-(Gd). By evaluation of the FFT pattern, it was determined that the zone axis of the examined xenotime-(Gd) single crystal is [11$\bar{1}$].

A Xenotime-(Gd) single crystal oriented in the [11$\bar{1}$] direction was also characterised using atomic-scale resolution imaging. Atomic-resolution HAADF STEM (Z contrast) and BF STEM images display the distribution of atomic columns in the tetragonal crystal structure of xenotime-(Gd) oriented along the [11$\bar{1}$] zone axis (Fig. 3). Bright spots in HAADF STEM image (Fig. 3a) represent
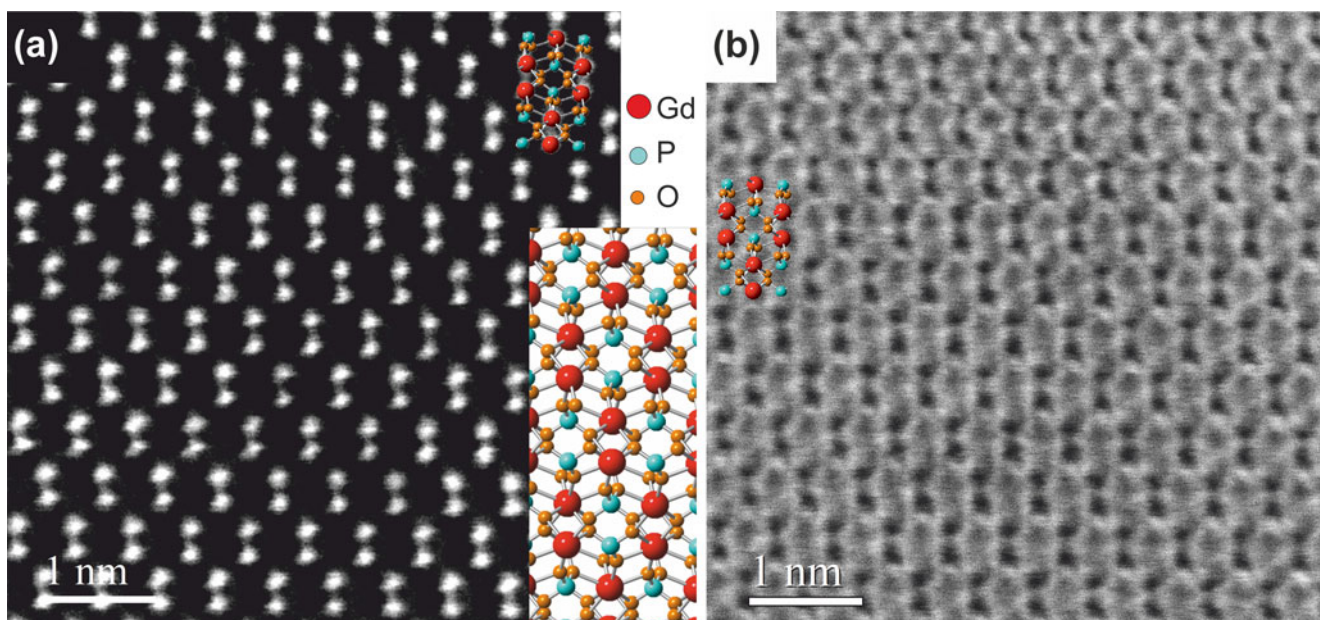

Figure 3. (a) Atomic-resolution HAADF STEM image of a xenotime-(Gd) single crystal observed along the [11$\bar{1}$] direction. The superimposed atomic structural model (bottom right) viewed along the [11$\bar{1}$] direction identifies the Gd atomic columns (red) in a xenotime-(Gd) single crystal. (b) A simultaneously recorded atomic-resolution BF STEM image of a xenotime-(Gd) single crystal observed from the [11$\bar{1}$] direction. Dark spots represent Gd atomic columns.

Gd atomic columns, which is concordant with a superimposed tetragonal crystal structure representation of xenotime oriented in the [11$\bar{1}$] direction. Gadolinium atomic columns appear dark in the simultaneously recorded atomic resolution BF STEM image (Fig. 3b).

It can be assumed that the unit-cell parameters of the observed mineral correspond to the weighted average of the corresponding end-members unit-cell parameters. The unit-cell parameters of synthetic REEPO$_4$ with a xenotime structure display a near-ideal linear trend of increasing unit-cell parameters with increasing ionic radii of REE cations. Moreover, the content of other possible substituents (U, Th, Ca, Si and As), which could alter the linear trend, is very low in the xenotime-(Gd) sample and, therefore, the influence of these elements is negligible for the cell-parameter calculation. The following are the calculated mean unit-cell parameters for studied xenotime-(Gd) from the weighted sum of end-members: $a = 6.9319(4)$ Å, $c = 6.0697(5)$ Å, $V = 291.66(1)$ Å^3 and $Z = 4$.

The refined and calculated unit-cell parameters are in very good agreement. Moreover, the empirical unit-cell parameters obtained from the FFT are slightly lower than the unit-cell parameters of synthetic analogues of xenotime-(Gd) of Rodriguez-Liviano et al. (2013) and Clavier et al. (2018), which reflects the presence of other REE with smaller ionic radii (Table 4).

Raman spectroscopy

The Raman spectra of xenotime-(Gd) and Gd-poor xenotime-(Y) have been documented previously in Ondrejka et al. (2023c). These spectra are influenced significantly by the photoluminescence (PL) of REE^{3+}, masking Raman signals in the low-frequency range (100–750 cm^{-1}) (see Fig. 4). Despite the intense PL, specific bands can be discernible in xenotime-(Y) at 650, 580 and 484 cm^{-1}, and in xenotime-(Gd) at 640, 576–577 and 483 cm^{-1}. The Raman modes become clearly distinguishable between 800 and 1200 cm^{-1} in both spectra excited by 532 nm and 633 nm lasers. Xenotime-(Y) exhibits distinctive bands centred at 999, 1024 and 1057 cm^{-1}, while the spectra of xenotime-(Gd) display lines at 994–996, 1018 and 1052 cm^{-1}, along with an additional, less intense band at 965 cm^{-1}, and minor broad features at approximately 870, 900 and 1150 cm^{-1}.

The positions of the Raman bands for xenotime-(Gd) align with previously reported data on xenotime-type orthophosphates (Begun et al., 1981; Lenz et al., 2015; Švecová et al., 2016; Yahiaoui et al., 2017; Lösch et al., 2019; Clavier et al., 2018). Generally, lattice vibration modes manifest below 300 cm^{-1} (Begun et al., 1981; Lösch et al., 2019) or up to 400 cm^{-1} (Clavier et al., 2018) encompassing translations and rotation modes of the entire (PO$_4$)$^{3-}$ unit. According to this literature, bands in the spectral range of 950–1100 cm^{-1} relate to the P–O symmetric and antisymmetric stretching modes of (PO$_4$)$^{3-}$

(Table 5). The frequencies observed for xenotime-(Gd) are lower than those for xenotime-(Y), aligning with the shifting positions of v_1 and v_3 observed in experimental studies on REE substitutions in xenotime-type orthophosphates (Begun et al., 1981; Clavier et al., 2018). Peaks at 965 cm^{-1}, 900 and 1150 cm^{-1} tentatively associate with Si and As substitution in an anion position in natural xenotime, necessitating further detailed examination. The strong PL is caused by the presence of Er^{3+} and Ho^{3+} (under 633 nm excitation), and by Er^{3+}, Eu^{3+}, Ho^{3+} and Sm^{3+} (under 532 nm excitation) (Fig. 4). Notably, Sm^{3+} probably contributes to the broadening of the 1017 cm^{-1} band, and the faint, broad band around 1150 cm^{-1} is possibly attributed to this luminescent centre (Lenz et al., 2015). Despite the Raman signal being overshadowed by PL, we deduce the absence of structural H$_2$O or (OH)$^-$ in xenotime-(Gd) because of the absence of bands within the stretching modes range of these groups after 633 nm excitation.

Discussion

Xenotime-(Gd) is a new lanthanide orthophosphate mineral of the xenotime group with a natural unique Gd-dominance over the other REE cations. It represents only the third Gd-dominant mineral, described in Nature, and approved by IMA-CNMNC (Pasero, 2024), after lepersonnite-(Gd), CaGd$_2$(UO$_2$)$_{24}$(SiO$_4$)$_4$(CO$_3$)$_8$(OH)$_{24}$·48H$_2$O, from the Shinkolobwe uranium deposit, DR Congo (Deliens and Piret, 1982) and cogenetic dimorphous monazite-(Gd) from the Zimná Voda occurrence near Prakovce, Slovakia (Ondrejka et al., 2023b). However, xenotime-(Gd) contains a significantly higher content of Gd: ≤29.3 wt.% Gd$_2$O$_3$, in comparison to lepersonnite-(Gd) (only 2.1 wt.% Gd$_2$O$_3$; Deliens and Piret, 1982) and monazite-(Gd) ≤23.4 wt.% Gd$_2$O$_3$ (Ondrejka et al., 2023b). Consequently, xenotime-(Gd) contains the highest Gd concentration among approved minerals. We emphasise the use of appropriate and precise analytical methods in these data, as there are other published data that document the possible presence of other Gd-dominant 'minerals', unfortunately without suitable analytical method or measurements. The presence of Gd-dominant 'monazite' with 42.5 wt.% Gd$_2$O$_3$ and an empirical formula (Gd$_{0.55}$Y$_{0.25}$Dy$_{0.1}$Sm$_{0.05}$Nd$_{0.05}$Th$_0$Ca$_0$)(PO$_4$) is noted from alkali-feldspar syenite pegmatite at the Myan Gyi mine, near Mogok, Myanmar (Kartashov, web data at mineralienatlas.de; mindat.org); however, with no further information. The impressive REE accumulations in lignite coals from the Russian Far East Pavlovka deposit contain fine-grained authigenic unknown Gd- and Dy-dominant minerals (Seredin, 1996). Several nano- to micro-sized particles of Gd–Ti–Zr oxides with dominant Gd occupancy and 9−57 wt.% Gd$_2$O$_3$ were identified in the lunar regolith from Mare Crisium (Bogatikov et al., 2004; Mokhov et al., 2011). In addition, an unnamed

Table 4. Unit-cell parameters for natural xenotime-(Y) and xenotime-(Gd) compared to the published data for synthetic xenotime compounds.

| Sample	Sample (method) / Reference	a (Å)	c (Å)	V (Å^3)
ZV-2 Xtm-(Gd)	xenotime-(Gd) (FFT pattern)	6.9589(5)	6.0518(6)	293.07(3)
ZV-2 Xtm-(Gd)	xenotime-(Gd) (calc.)	6.9319(4)	6.0697(5)	291.66(1)
GdPO$_4$ tetragonal, synthetic	Celebi and Kolis (2002)	6.969	6.095	296.02
GdPO$_4$ tetragonal, synthetic	Rodriguez-Liviano et al. (2013)	6.9648(4)	6.1050(5)	296.14
GdPO$_4$ tetragonal, synthetic	Clavier et al. (2018)	6.9612(7)	6.1026(10)	295.72
YPO$_4$ tetragonal, synthetic	Ushakov et al. (2001)	6.8832(3)	6.0208(4)	285.26
Xenotime-(Y)	Strunz and Nickel (2001)	6.89	6.04	286.73
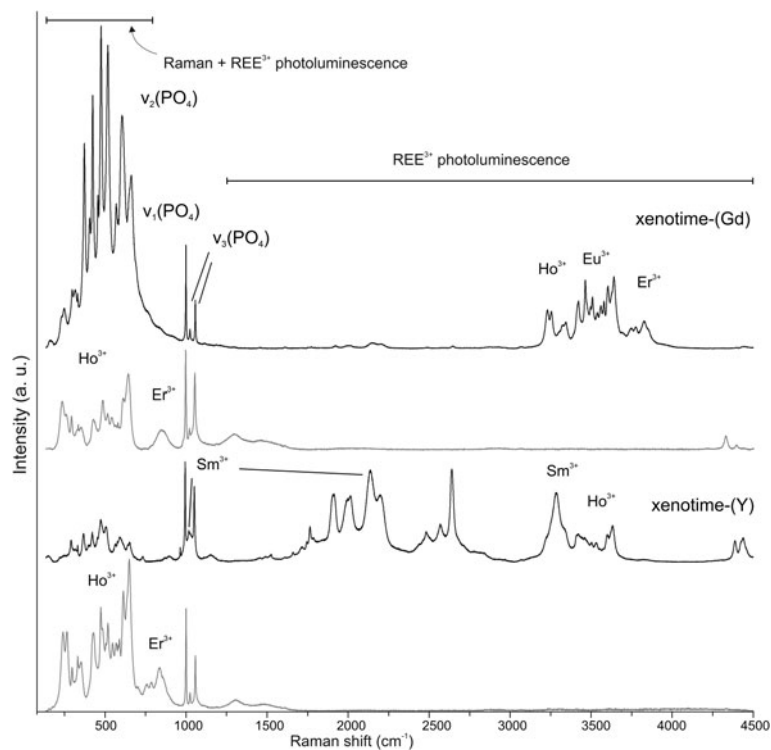
Figure 4. Depolarised Raman spectra captured for both natural xenotime-(Y) and xenotime-(Gd) (Prakovce, Zimná Voda ZV-2 sample) using two distinct laser excitations: 532 nm (black line, upper) and 633 nm (grey line, lower). The spectra are annotated with labelled sections indicating regions of photoluminescence (PL) and Raman bands. The intensity scale bar is provided in arbitrary units (a. u.).

Gd-dominant mineral (Gd > Ce > La) close to the $Gd_2Ti_4O_{11}$ formula was noted from fumaroles in the active Kudriavy Volcano, Kuril Islands, Russia (Bogatikov *et al.*, 2004). However, all the above-mentioned findings of possible Gd-dominant minerals need to be taken and interpreted with caution, because the data were obtained using semiquantitative EDX analysis without appropriate analytical details available. Furthermore, other analytical data (e.g, XRD, micro-Raman) are lacking.

Beside xenotime-(Gd), xenotime-(Y) from the Zimná Voda REE–U–Au occurrence is also enriched in Gd (11.6 to 27.9 wt.% Gd_2O_3, 0.13 to 0.35 apfu Gd). Moreover, inclusions of xenotime-(Gd), monazite-(Gd) and monazite-(Sm) (≤50 μm in size) with up to 29.8 wt.% Gd_2O_3 (≤0.38 apfu Gd) have been found recently in spessartine garnet in the Otov rare-element granitic metapegmatite (beryl–columbite-phosphate subtype), Czech Republic (Vrtiška, Ondrejka and Uher, unpubl. data). Rare occurrences of Gd, Dy-rich and Yb-dominant compositions in the xenotime-group minerals have also been described from some magmatic and metamorphic-hydrothermal systems (Demartin *et al.*, 1991; Förster and Rhede, 1995; Förster, 1998;

Buck *et al.*, 1999; Masau *et al.*, 2000; Franz *et al.*, 2015). In addition to Prakovce-Zimná Voda, the highest published Gd_2O_3 content in xenotime-(Y) attains 25 wt.% (0.31 apfu Gd), from the quartz vein of Au–REE mineralisation in the Subpolar Urals, Russia (Repina, 2010, 2011).

Such unusual enrichment of Gd in xenotime-(Gd) as well as in some other REE minerals [e.g. monazite-(Gd), hingganite-(Y)] and the progressive development of a MREE enhanced signature could be a result of local selective complexing of REE during granite to pegmatite sequence solidification in aqueous F–Cl– Li–CO₂-bearing fluids (Masau *et al.*, 2002; Twardak *et al.*, 2023). Moreover, hydrothermal xenotime-(Gd) and associated Gd-rich minerals precipitated in response to the alteration of MREE-selective, but nominally REE-free uraninite, brannerite and fluorapatite precursors by low-temperature hydrothermal fluids. Further details and description of Gd-MREE-enriched minerals in the Prakovce-Zimná Voda occurrence can be found in Ondrejka *et al.* (2023c).

The existence of $GdPO_4$ and mixed $Gd_xLn_{1-x}PO_4$ dimorphism has been experimentally replicated and the kinetic-thermodynamic (meta)stability of the monazite and zircon structure types under various *P-T* conditions has been described in the literature (e.g. Mullica *et al.*, 1990; Celebi and Kolis, 2002; Kolitsch and Holtstam, 2004; Rodriguez-Liviano *et al.*, 2013; Hay *et al.*, 2013; Hefferman *et al.*, 2016; Meng *et al.*, 2016; Li *et al.*, 2018; Muñoz and Rodríguez-Hernández, 2018; and references therein). There is a general consensus that the structural boundary between monazite and xenotime usually lies between Gd and Tb (e.g. Ni *et al.*, 1995; Gratz and Heinrich, 1998; Hay *et al.*, 2013; Rodriguez-Liviano *et al.*, 2013). The investigation of natural $GdPO_4$ orthophosphates from Prakovce, Zimná Voda (Ondrejka *et al.*, 2023b, 2023c) confirms the possibility of (1) substantial Gd incorporation into REE-selective structures and (2) the stabilisation of Gd-dominant orthophosphate with a zircon/xenotime-type structure by substitution of smaller HREE+Y cations in the *A* site

Table 5. Raman bands for xenotime-(Gd).

Bands (cm^{-1})	Symmetry	Assignment
<400	$B_{1g}+E_g$	Lattice (T, R)
483	A_{1g}	$\nu_2[PO_4]$
576–577	E_g	$\nu_4[PO_4]$
640	B_{1g}	$\nu_4[PO_4]$
994–996	A_{1g}	$\nu_1[PO_4]$
1018	E_g	$\nu_3[PO_4]$
1052	B_{1g}	$\nu_3[PO_4]$

Notes: ν1 and ν3 – symmetric and antisymmetric stretching; ν2 and ν4 – symmetric and antisymmetric bending. Lattice modes: T – translation, R – rotation; REE photoluminescence bands not included.

(Mullica *et al.*, 1986, 1990; Gratz and Heinrich, 1998; Clavier *et al.*, 2011; Rodriguez-Liviano *et al.*, 2013; Ondrejka *et al.*, 2023c). The stabilisation of the monazite- *versus* xenotime-type structure of the natural REEPO$_4$ species depends on the average REE^{3+} ionic radius (Kolitsch and Holtstam, 2004). In addition, the xenotime-(Gd) − monazite-(Gd) pair represents the first naturally occurring dimorphism among the known REE phosphates.

References

Åmli R. and Griffin W.L. (1975) Microprobe analysis of REE minerals using empirical correction factors. *American Mineralogist*, **60**, 599–606.

Anthony J.W., Bideaux R.A., Bladh K.W. and Nichols M.C. (editors) (2024) *Handbook of Mineralogy*. Mineralogical Society of America, Chantilly, VA 20151-1110, USA. http://www.handbookofmineralogy.org/ (visited 17 August 2024).

Bajaník Š., Hanzel V., Mello J., Pristaš J., Reichwalder P., Snopko L., Vozár J. and Vozárová A. (1983) *Explanation to Geological Map of the Slovenské Rudohorie Mts.—Eastern part, 1:50 000*, 223 pp. State Geological Institute of D. Štúr, Bratislava [in Slovak].

Bayliss P. and Levinson A.A. (1988) A system of nomenclature for rare-earth mineral species: Revision and extension. *American Mineralogist*, **73**, 422–423.

Begun G.M., Beall G.W., Boatner L.A. and Gregor W.J. (1981) Raman spectra of the rare earth orthophosphates. *Journal of Raman Spectroscopy*, **11**, 273–278.

Bogatikov O.A., Mokhov A.V., Kartashov P.M., Magazina L.O., Koporulina E.V., Ashikhmina N.A. and Gorshkov A.I. (2004) Selectively Gd-enriched micro- and nano-sized minerals in the lunar regolith from the Crisium Mare. *Doklady Akademii Nauk*, **394**, 81–84 [in Russian].

Buck H.M., Cooper M.A., Černý P., Grice J.D., and Hawthorne F.C. (1999) Xenotime-(Yb), YbPO$_4$, a new mineral species from the Shatford lake pegmatite group, Southeastern Manitoba, Canada. *The Canadian Mineralogist*, **37**, 1303–1306.

Celebi A.S. and Kolis J.W. (2002) Hydrothermal synthesis of xenotime-type gadolinium orthophosphate. *Journal of the American Ceramic Society*, **85**, 253–254.

Clavier N., Podor R. and Dacheux N. (2011) Crystal chemistry of the monazite structure. *Journal of the European Ceramic Society*, **31**, 941–976.

Clavier N., Mesbah A., Szenknect S. and Dacheux N. (2018) Monazite, rhabdophane, xenotime and churchite: Vibrational spectroscopy of gadolinium phosphate polymorphs. *Spectrochimica Acta Part A: Molecular and Biomolecular Spectroscopy*, **205**, 85–94.

Deliens M. and Piret P. (1982) Bijvoetite et lepersonnite carbonates hydratés d'uranyle et des terres rares de Shinkolobwe, Zaïre. *The Canadian Mineralogist*, **20**, 231–238 [in French].

Demartin F., Pilati T., Diella V., Donzelli S., Gentile P. and Gramaccioli C.M. (1991) The chemical composition of xenotime from fissures and pegmatites in the Alps. *The Canadian Mineralogist*, **29**, 69–75.

Downs R.T. and Hall-Wallace M. (2003) The American Mineralogist Crystal Structure Database. *American Mineralogist* 88, 24–250.

Ferenc Š., Števko M., Mikuš T., Milovská S., Kopáčik R. and Hoppanová E. (2021) Primary minerals and age of the hydrothermal quartz veins containing U-Mo-(Pb, Bi, Te) mineralization in the Majerská valley near Čučma (Gemeric Unit, Spišsko-Gemerské Rudohorie Mts., Slovak Republic). *Minerals*, **11**, 629.

Förster H.-J. (1998) The chemical composition of REE-Y-Th-U-rich accessory minerals in peraluminous granites of the Erzgebirge–Fichtelgebirge region, Germany. Part II: Xenotime. *American Mineralogist*, **83**, 1302–1315

Förster H.-J. and Rhede D. (1995) Composition of monazite and xenotime from the Fichtelgebirge granites—an electron microprobe study. *Berichte der Deutschen Mineralogischen Gesellschaft. Beihefte zum European Journal of Mineralogy*, **7**, 68 [Conference proceedings].

Franz G., Andrehs G. and Rhede D. (1996) Crystal chemistry of monazite and xenotime from Saxothuringian-Moldanubian metapelites, NE Bavaria, Germany. *European Journal of Mineralogy*, **8**, 1097–1118.

Franz G., Morteani G. and Rhede D. (2015) Xenotime-(Y) formation from zircon dissolution–precipitation and HREE fractionation: An example from a metamorphosed phosphatic sandstone, Espinhaço fold belt (Brazil). *Contributions to Mineralogy and Petrology*, **170**, 37.

Gratz R. and Heinrich W. (1998) Monazite-xenotime thermometry. III. Experimental calibration of the partitioning of gadolinium between monazite and xenotime. *European Journal of Mineralogy*, **10**, 579–588.

Hay R.S., Mogilevsky P. and Boakye E. (2013) Phase transformations in xenotime rare-earth orthophosphates. *Acta Materialia*, **61**, 6933–6947.

Hefferman K.M., Ross N.L., Spencer E.C. and Boatner L.A. (2016) The structural response of gadolinium phosphate to pressure. *Journal of Solid State Chemistry*, **241**, 180–186.

Ivanička J., Snopko L., Snopková P. and Vozárová A. (1989) Gelnica group–Lower unit of Spišsko-Gemerské Rudohorie Mts. (West Carpathians), Early Paleozoic. *Geologica Carpathica*, **40**, 483–501.

Kohút M. and Stein H. (2005) Re-Os molybdenite dating of granite-related Sn-W-Mo mineralisation at Hnilec, Gemeric Superunit, Slovakia. *Mineralogy and Petrology*, **85**, 117–129.

Kolitsch U. and Holtstam D. (2004) Crystal chemistry of REEXO$_4$ compounds (X = P, As,V). II. Review of REEXO$_4$ compounds and their stability fields. *European Journal of Mineralogy*, **16**, 117–126.

Lenz Ch., Nasdala L., Talla D., Hauzenberger Ch., Seitz R. and Kolitsche U. (2015) Laser induced REE^{3+} photoluminescence of selected accessory minerals — An "advantageous artefact" in Raman spectroscopy. *Chemical Geology*, **415**, 1–16.

Levinson A.A. (1966) A system of nomenclature for rare-earth minerals. *American Mineralogist*, **51**, 152–158.

Li W., Ding X., Meng C., Ren Ch., Wu H. and Yang H. (2018) Phase structure evolution and chemical durability studies of Gd$_{1-x}$Yb$_x$PO$_4$ ceramics for immobilization of minor actinides. *Journal of Material Science*, **53**, 6366–6377.

Lösch H., Hirsch A., Holthausen J., Peters L, Xiao B., Neumeier S., Schmidt M. and Huittinen, N. (2019) A spectroscopic investigation of Eu^{3+} Incorporation in LnPO$_4$ (Ln = Tb, Gd$_{1-x}$Lu$_x$, X = 0.3, 0.5, 0.7, 1). *Ceramics, Frontiers in Chemistry*, **7**, 94.

Mandarino J.A. (1979) The Gladstone-Dale relationship. Part III. Some general applications. *The Canadian Mineralogist*, **17**, 71–76.

Mandarino J.A. (1981) The Gladstone-Dale relationship. Part IV. The compatibility concept and its application. *The Canadian Mineralogist*, **19**, 441–450.

Masau M., Černý P. and Chapman R. (2000) Dysprosian xenotime-(Y) from the Annie Claim #3 granitic pegmatite, Southeastern Manitoba, Canada: Evidence of the tetrad effect? *The Canadian Mineralogist*, **38**, 899–905.

Masau M., Černý P., Cooper M.A., Chapman R. and Grice J.D. (2002) Monazite-(Sm), a new member of the monazite group from the Annie Claim #3 granitic pegmatite, Southeastern Manitoba. *The Canadian Mineralogist*, **40**, 1649–1655.

Meng C., Ding X., Zhao J., Li W., Ren C. and Yang H. (2016) Preparation and characterization of cerium-gadolinium monazites as ceramics for the conditioning of minor actinides. *Progress in Nuclear Energy*, **89**, 1–6.

Miyawaki R. and Nakai I. (1993) Crystal structures of rare earth minerals. Pp. 249–518 in: *Handbook on the Physics and Chemistry of Rare Earths*, Vol.16., Chapter 108 (Gschneidner K. A. Jr. and Eyring L., editors). Elsevier Science Publishers B.V., Amsterdam.

Mokhov A.V., Kartashov P.M., Gornostaeva T.A., Bogatikov O.A. and Ashikhmina T.A. (2011) New phases of lanthanoids and actinoids from the regolith samples delivered by the Luna-24. *Doklady Earth Sciences*, **437**, 479–482.

Mullica D.F., Grossie D.A. and Boatner L.A. (1986) Crystal structure of 1:1 gadolinium/ytterbium orthophosphate. *Inorganica Chimica Acta*, **118**, 173–176.

Mullica D.F., Sappenfield E.L. and Boatner L.A. (1990) A structural investigation of several mixed lanthanide orthophosphates. *Inorganica Chimica Acta*, **174**, 155–159.

Muñoz A. and Rodríguez-Hernández P. (2018) High-pressure elastic, vibrational and structural study of monazite-type $GdPO_4$ from ab initio simulations. *Crystals*, **8**, 209.

Ni Y., Hughes J.M. and Mariano A.N. (1995) Crystal chemistry of the monazite and xenotime structures. *American Mineralogist*, **80**, 21–26.

Novotný L. and Čížek P. (1979) New occurrence of uranium and gold, southern from Prakovce in Spišsko-gemerské Rudohorie Mts. *Mineralia Slovaca*, **11**, 188–190. [In Slovak]

Ondrejka M., Ferenc Š., Majzlan J., Števko M., Kopáčik R., Voleková B., Milovská S., Göttlicher J., Steininger R., Mikuš T., Uher P., Biroň A., Sejkora J. and Molnárová A. (2023a) Secondary uranyl arsenates–phosphates and Sb–Bi-rich minerals of the segnitite–philipsbornite series in the oxidation zone at the Prakovce-Zimná Voda REE–U–Au quartz-vein mineralisation, Western Carpathians, Slovakia, *Mineralogical Magazine*, **87**, 849–865.

Ondrejka M., Uher P., Ferenc Š., Majzlan J., Pollok K., Mikuš T., Milovská S., Molnárová A., Škoda R., Kopáčik R., Kurylo S. and Bačík P. (2023b) Monazite-(Gd), a new Gd-dominant mineral of the monazite group from the Zimná Voda REE–U–Au quartz vein, Prakovce, Western Carpathians, Slovakia, *Mineralogical Magazine*, **87**, 568–574.

Ondrejka M., Uher P., Ferenc Š., Milovská S., Mikuš T., Molnárová A., Škoda R., Kopáčik R. and Bačík P. (2023c) Gadolinium-dominant monazite and xenotime: selective hydrothermal enrichment of middle REE during low-temperature alteration of uraninite, brannerite and fluorapatite (the Zimná Voda REE–U–Au quartz vein, Western Carpathians, Slovakia), *American Mineralogist*, **108**, 754–768.

Ondrejka M., Bačík P., Majzlan J., Uher P., Ferenc Š., Števko M., Čaplovičová M., Milovská S., Mikuš T., Rößler C., Matthes C. and Molnárová A. (2024) Xenotime-(Gd), IMA 2023-091. CNMNC Newsletter 77. *Mineralogical Magazine*, **88**, https://doi.org/10.1180/mgm.2024.5

Pasero M. (2024) The New IMA List of Minerals. International Mineralogical Association. Commission on new minerals, nomenclature and classification (IMA-CNMNC). http://cnmnc.units.it/

Repina S.A. (2010) Zoning and sectoriality of the florencite and xenotime group minerals from quartz veins, the Subpolar Urals. *Geology of Ore Deposits*, **52**, 821–836.

Repina S.A. (2011) Fractionation of REE in the xenotime and florencite paragenetic association from Au-REE mineral occurrences of the Nether-Polar Urals. *Geochemistry International*, **49**, 868–887.

Repina S.A., Khiller V.V. and Makagonov E.P. (2014) Microheterogeneity of crystal growth zones as a result of REE fractionation. *Geochemistry International*, **52**, 1057–1071.

Rodriguez-Liviano S., Becerro A.I., Alcántara D., Grazú V., de la Fuente J.M. and Ocaña M. (2013) Synthesis and properties of multifunctional tetragonal $Eu:GdPO_4$ nanocubes for optical and magnetic resonance imaging applications. *Inorganic Chemistry*, **52**, 647–654.

Rojkovič I., Háber M. and Novotný L. (1997) U-Au-Co-Bi-REE mineralization in the Gemeric unit (Western Carpathians, Slovakia). *Geologica Carpathica*, **48**, 303–313.

Rojkovič I., Konečný P., Novotný L., Puškelová Ľ. and Streško V. (1999) Quartz-apatite-REE vein mineralization in Early Paleozoic rocks of the Gemeric Superunit, Slovakia. *Geologica Carpathica*, **50**, 215–227.

Seredin V.V. (1996) Rare earth element-bearing coals from the Russian Far East deposits. *International Journal of Coal Geology*, **30**, 101–129.

Strunz, H. and Nickel E.H. (2001) Strunz Mineralogical Tables, 9th Edition. Berlin and Stuttgart (E. Schweizerbart'sche Verlagsbuchhandlung), 870 pp.

Švecová E., Čopjaková R., Losos Z., Škoda R., Nasdala L. and Cícha J. (2016) Multi-stage evolution of xenotime–(Y) from Písek pegmatites, Czech Republic: an electron probe micro-analysis and Raman spectroscopy study. *Mineralogy and Petrology*, **110**, 747–765.

Twardak D., Pieczka A., Kotowski J. and Nejbert K. (2023) Mineral chemistry and genesis of monazite-(Sm) and monazite-(Nd) from the Blue Beryl Dyke of the Julianna pegmatite system at Piława Górna, Lower Silesia, Poland. *Mineralogical Magazine*, **87**, 575–581.

Ushakov S.V., Helean K.B., Navrotsky A. and Boatner L.A. (2001) Thermochemistry of rare-earth orthophosphates. *Journal of Materials Research*, **16**, 2623–2633.

Vegard L. (1927) XLVII. The structure of xenotime and the relation between chemical constitution and crystal structure. *The London, Edinburgh, and Dublin Philosophical Magazine and Journal of Science*, **7**, 4, 22, 511–525.

Villaseñor G., Catlos E.J., Broska I., Kohút M., Hraško Ľ., Aguilera K., Etzel T.M., Kyle R. and Stockli D.F. (2021) Evidence for widespread mid-Permian magmatic activity related to rifting following the Variscan orogeny (Western Carpathians). *Lithos*, **390–391**, 106083.

Warr L.N. (2021) IMA-CNMNC approved mineral symbols. *Mineralogical Magazine*, **85**, 291–320.

Yahiaoui Z., Hassairi M. and Dammak M. (2017) Synthesis and optical spectroscopy of $YPO_4:Eu^{3+}$ orange–red phosphors. *The Journal of Electronic Materials*, **46**, 4765–4773.